A Deployable Multifunctional Sensor for a Catheter Device for the Renal Denervation of Resistant Hypertension

Ruiqi Lim, Ramona Damalerio, Musafargani Sikkandhar, James Yap,
Eul Joon Park, Ran Young Lim, In Hee Bae and Ming-Yuan Cheng†

***Abstract*— This study developed a deployable multimodal and multifunctional sensor for a catheter device for renal denervation procedures to treat resistant hypertension. The catheter device has three deployable spines. When the device is deployed, it can be used to perform ablation of the renal nerve, detect the contact force exerted by the device on the renal artery wall, measure the temperature of the ablation sites, and provide feedback to control the ablation power. Each spine comprises a microelectromechanical system (MEMS) multimodal sensor chip, contact force sensor, 100-µm-thick tungsten foil for radiopacity, and shape memory alloy spine. The MEMS chip has a platinum-based resistance temperature detector (Pt RTD) integrated with a radiofrequency (RF)-powered heating electrode. It can withstand 32 ablation cycles with an RF generator setting of 8 W for 60 s per ablation cycle. An ex vivo ablation study demonstrated that an RF power range of 1–1.5 W achieved optimal ablation lesions. The Pt RTD or temperature sensor has a sensing range of 25°C–94°C and sensing response time of < 0.5s. The contact force sensor has a sensing range of 50–500 mN, with a minimum resolution of 50 mN and hysteresis error of 0.7 kΩ. In benchtop studies, the force sensor performed well during catheter deployment under three conditions: in air, in a hollow tube, and in saline solution. During catheter activation, the force sensor can detect the contact force between the tube wall and force-sensor module. The force-sensor resistance readout is consistent for both the hollow tube and saline solution.**

***Index Terms*— renal denervation, catheter, contact force sensor, temperature sensor, MEMS, FPCB**

I. Introduction

THERAPY-resistant hypertension is a condition in which patients do not respond to aggressive medication regimes that include the concurrent use of two types of antihypertensive medications and one type of diuretic [1], [2]. The incidence rate for developing resistant hypertension is approximately 1.9%, with a prevalence of less than 10% among patients with hypertension [3], [4]. Patients with resistant hypertension have an increased risk of developing stroke, cardiovascular disease, kidney failure, and obesity compared with patients with hypertension [5]-[15]. The common causes of resistant hypertension include excessive salt intake, obesity, alcohol consumption, and medical conditions such as endocrine and neurological disorders [4]-[14].

In recent years, interventional approaches, such as renal denervation (RDN) and carotid baroreceptor activation therapy (BAT) have been explored as potential treatments for resistant hypertension. Carotid BAT devices activate the carotid baroreceptor through either electrical stimulation or the mechanical expansion of the carotid artery [16]. The activated baroreceptor then sends a signal to the brain, which is registered as an increase in blood pressure. The brain then sends a signal to organs such as the heart, kidney, and blood vessels to regulate and control the blood pressure to be at a desired level [16]-[21]. The Barostim Neo System uses implanted pulse generators to generate an electrical pulse to activate the baroreceptor. Clinical studies reported a reduction in blood pressure at 6-months postsurgery with no safety concerns. This demonstrated the feasibility of the procedure as a treatment for resistant hypertension [20], [21]. Another device, MobiusHD, involving the implantation of an endovascular graft to expand the carotid artery for baroreceptor activation, yielded a reduction in blood pressure in patients with resistant hypertension [20], [22], [23]. Currently, clinical studies are validating the safety and efficacy of the MobiusHD system [23]. Thus, BAT has potential for treating resistant hypertension. However, this therapy approach is invasive because the device must be implanted for electrical stimulation or artery expansion.

RDN procedures involve the insertion of a catheter into a renal artery for nerve ablation. The renal denervation catheter comprises radiofrequency (RF) ablation electrodes and temperature sensors. Upon reaching the site of interest, the catheter is activated to allow the ablation electrodes to maintain contact with the tissue wall. An external generator

This work was supported by A*ccelerate Technologies Pte Ltd, the commercialization arm of the Agency for Science, Technology and Research (A*STAR) under Decentralised GAP Grant Ref. No. ACCL/19-GAP034-R20H

Ruiqi Lim, Maria Ramona Ninfa Bautista Damalerio and Ming-Yuan Cheng are with the MedTech Department of Institute of Microelectronics, A*STAR (Agency for Science, Technology and Research), Singapore 117685 / †correspondence email: chengmyn@gmail.com.

Eul Joon Park, Ran Young Lim and In Hee Bae are with Kalos Medical Inc., Suwon-si Gyeonggi-do 16506 South Korea

provides the RF energy to enable the ablation of the renal nerve. This ablation procedure decreases the sympathetic signaling to the kidneys, increases blood flow in the artery, and helps keep the blood pressure at a desired level [24-25]. The global market size for RDN devices is approximately USD 41.7 million, with a growth rate of 42.3% expected by 2026. In 2017, RF-based RDN devices held the largest market share at 75% [26]. Recently, a 3-year follow-up on clinical studies reported favorable results in blood pressure reduction with no long-term safety concerns [27].

In this paper, a deployable multimodal and multifunctional sensor for a catheter device for RDN procedures to treat therapy-resistant hypertension is presented. The proposed catheter device has an integrated microelectromechanical system (MEMS)-based temperature sensor and ablation electrode and an additional printable force sensor. The additional force sensor is designed to improve the procedure success rate by ensuring strong contact between the heater electrodes and tissue wall before nerve ablation. The details of the sensor design, prototype assembly, and benchtop characterization results are presented.

II. Design Concept

The design concept and device packaging developed in this study involve three deployable multifunctional sensor modules integrated in a single wire-guided ablation catheter forming an RDN catheter. The main components for each multifunctional sensor module are a MEMS-based sensor chip—which is integrated with an RF ablation electrode—and temperature [28] and printable force sensors. The multifunction sensor module is assembled on a memory alloy spine structure to form the RDN device. The RDN catheter is inserted into the patient's renal artery for the RDN procedure (Fig. 1).

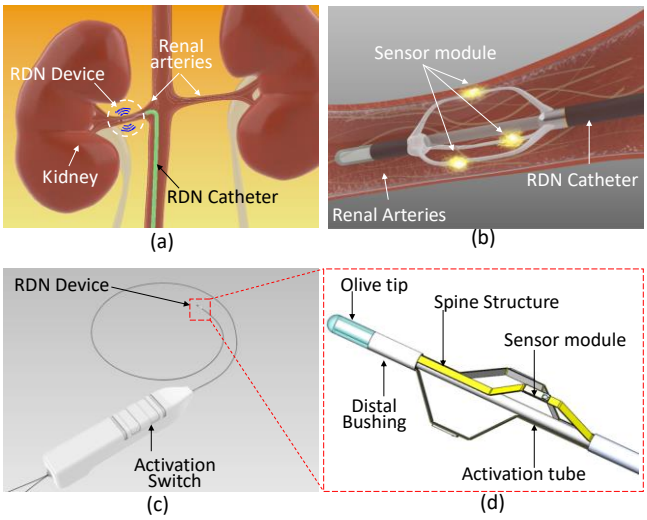

Fig. 1. Renal denervation (RDN) procedure. (a) Insertion of the RDN catheter into the renal arteries; (b) schematic of the activated RDN device in renal arteries for nerve ablation; (c) schematic of the RDN catheter; (d) schematic of the RDN device.

On reaching the site of interest, the RDN catheter is activated by a surgeon. The three RDN devices expand to allow the multifunctional sensor module to meet the tissue wall of the renal arteries (Fig. 1b). The force-sensing function of this multifunctional RDN catheter enables the surgeon to determine the quality of the contact between the heating electrodes and tissue wall. Subsequently, an external RF generator supplies RF energy to the RF ablation electrode for renal nerve ablation. During ablation, the temperature-sensing feature of the RDN device measures the ablation temperature and provides feedback to the external circuitry. This quantitative feedback is used to control the optimal RF output power required for effective nerve ablation. By ensuring strong contact and a real-time closed-loop feedback system for the RF energy and ablation temperature, a higher RDN success rate can be achieved and complications induced by high blood pressure can be reduced or prevented.

The MEMS-based sensor chip incorporates temperature sensing, a heater, and a printed force-sensing element stacked onto a flexible printed circuit board (FPCB) with interdigital metal traces. The MEMS-based sensor chip is electrically connected to the FPCB through wire bonding between the stacked chips. The sensor input and output signals from the FPCB to the external generator are then connected using four 1.5-m-length insulated wires. A 100-µm-thick radiopaque film is incorporated into the RDN device to determine its location under fluoroscopy imaging. The assembled parts are placed onto a memory alloy spine structure. This spine structure is bridge shaped for easy catheter activation. Fig. 2 depicts the stacked structure of the RDN device.

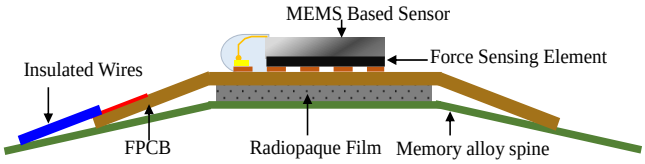

Fig. 2. RDN device stacked structure

A. Platinum-based Temperature Sensor

The temperature sensor designed as a MEMS-based resistance temperature detector (RTD) sensor chip has a sensing element made of metal. Its operation is based on a linear correlation between the metal and temperature sensor to enable the resistance of the RTD sensing element to increase as the temperature increases. Copper (Cu), gold (Au), and platinum (Pt) were evaluated as candidate materials for the sensing element; Pt was selected because of its biocompatibility, inert properties in air and water, and resistance to corrosion [29]. Pt also has a low temperature coefficient of resistance. The RTD sensing element has a width of 12 µm and a thickness of 0.15 µm. The initial RTD resistance has a baseline resistance of 1 kΩ at room temperature. The theoretical calculation of the Pt RTD indicates a relatively large change in resistance of >20%, from 20°C to 85°C.

B. Radiofrequency Heater Electrode

The heating or ablation electrode designed for the MEMS-based sensor chip is an RF ablation electrode. It is composed of 2.0 µm of Cu, 2.0 µm of nickel (Ni), 0.3 µm of Au, 0.05

μm of chromium (Cr), and 0.2 μm of Pt and is stacked directly above the temperature sensor with a dielectric layer. The Cu-Ni-Au multiple metal layer is designed to cater for the ablation requirement of maximum 8W applied RF energy. The thin-film platinum layer which is biocompatible has been selected as the surface electrode material to enable direct contact with the artery. The temperature sensor and RF-powered electrode are separated by a 1-μm dielectric layer. This allows the temperature at the ablation location to be measured when the RF electrode is in use. The RF-powered heating electrode can withstand 32 ablation cycles with an RF generator setting of up to 8 W for 60 s per ablation cycle.

C. Contact Force Sensor

To determine and quantify the degree of contact between the RF-powered electrodes with the renal artery wall, a contact force sensor is also incorporated in the device. The force sensor comprises a force-sensing element and interdigital electrode. The force-sensing element uses a conductive carbon based piezoresistive material with sheet resistance of 50Ω/square mil, AG 125 (MOS Corporation Ltd., Hong Kong), through which the resistance of the force-sensing element decreases exponentially with the amount of force applied. The contact force sensor is fabricated by printing a force-sensing element at the bottom of the MEMS-based sensor chip. Compared with the MEMS in-chip contact sensor, it uses the entire bottom of the MEMS-based sensor chip and maximizes the area of contact.

The interdigital electrode of the force sensor is fabricated on an FPCB. The MEMS-based sensor chip is stacked onto the FPCB, and the force-sensing element is positioned directly over the interdigital electrode. The contact force sensor is activated using tactile contact between the bottom of the MEMS-based sensor chip and the interdigitated metal traces of the FPCB. This stacking allows for the effective transfer of the contact force from the artery wall to the MEMS chip and force sensor.

III. Fabrication and Packaging

A. MEMS-based Sensor Chip Fabrication

The integrated MEMS-based sensor chip was fabricated using a standard semiconductor micromachine process and a five-mask fabrication process. The flowchart of the fabrication process is illustrated in Fig. 3.

First, a 1-μm layer of oxide is deposited onto a 750-μm-thick silicon wafer. The temperature sensor with a sensing element made of Pt is then formed. The target resistance value for the temperature sensor is 1,000 Ω. The fabrication of the Pt sensing element begins with a layer of photoresist (PR) that is spin coated onto the wafer, followed by a photolithography of the PR using Mask #1. A 50-nm-thick layer of Cr, which acts as an adhesive to attach the Pt to the oxide layer, is first evaporated onto the wafer, followed by a 0.15-μm layer of Pt. Subsequently, another 50-nm-layer of Cr is evaporated on top of the Pt layer to promote the adhesion of the Pt to the next dielectric oxide layer. The Cr–Pt–Cr layer is then lifted off to form the structure of the temperature sensor. After PR removal, the wafer undergoes an annealing process at 150°C to achieve the target sensing element resistance value of 1,000 Ω.

A stacked dielectric 1.5-μm-thick SiO_2 layer with 0.5 μm of SiN_x is used as a barrier layer to prevent Cu diffusion into the temperature sensor layer and silicon. This barrier layer is formed using a plasma-enhanced chemical vapor deposition process to deposit 1.5 μm of oxide, followed by 0.5 μm of nitride. PR is spin coated and patterned to form the bonding pad opening for the sensor chips using Mask #2. To expose the bonding pad region, 0.5 μm of nitride and 1.5 μm of oxide are etched, followed by a PR removal process.

In the next step, a Cu base material for the RF-powered electrode is formed. First, an adhesion layer of 0.1 μm of Cr followed by a seed layer of 0.2 μm of Cu are evaporated onto the wafers. The PR is spin coated and patterned with the RF electrode and contact pad structure using Mask #3. This is followed by an oxygen descum process. The wafers are then ready for the 2 μm of Cu, 2 μm of Ni, and 0.3 μm of Au that are used in the electroplating process. After electroplating, the PR is removed and a blanket wet etching process is conducted to remove the seed layer.

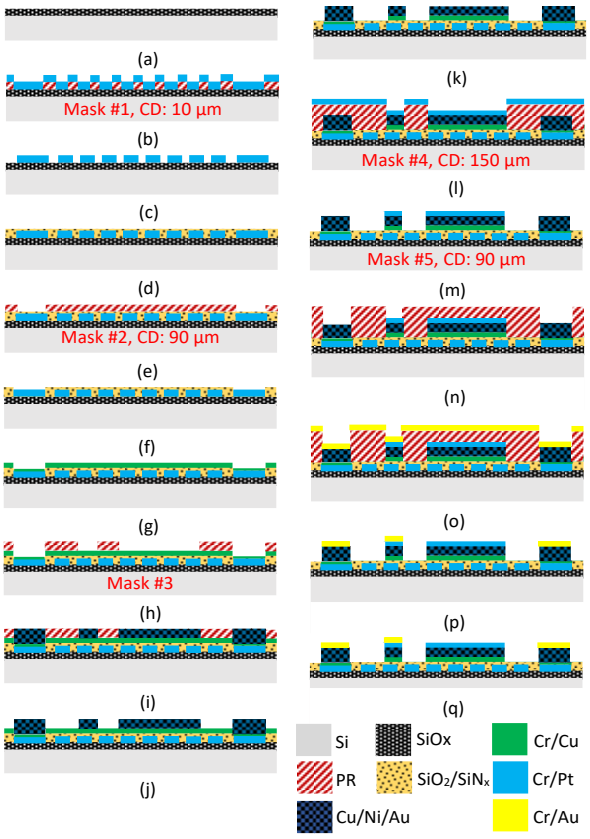

Fig. 3. Flowchart of the MEMS-based sensor chip fabrication process.

In the next process, Mask #4 is used to fabricate the Pt layer over the base Cu to achieve the final heating electrode. Specifically, 4.5 μm of PR is required for the Cu-based electrode. After PR lithography and patterning are complete, a layer of Cr (50 nm) and Pt (200 nm) is evaporated onto the wafer. In the next step, a lift-off process is performed to obtain an RF-powered heating electrode. After the completion of the

lift-off process, the next process involves the use of Mask #5 to form a bonding pad finish for the wire-bonding process. Again, a layer of PR is used for the lithography and patterning process. The surface of the wafer undergoes oxide cleaning and argon sputtering to prepare the wafer for Au deposition. A layer of Cr (20 nm) and Au (500 nm) is evaporated onto the wafers. The lift-off process is conducted to form the bonding pad finish. After PR removal, the wafer fabrication process is complete. The final mask process involves forming the bonding pad finish for the wire-bonding process. The PR from the previous step is first removed, and another layer of PR is spin coated onto the wafer. After lithography and patterning, the wafer can be thinned to 100 µm using a back-grinding process. It is then wafer sawn to reticle level and eventually into individual MEMS-based sensor chips with a length and width of 1.8 and 0.6 mm, respectively.

B. Catheter Assembly

After the fabrication of the MEMS-based sensor chip, the next process is to form the single spine structure. Figs. 4a and 4b present the assembled spine structures.

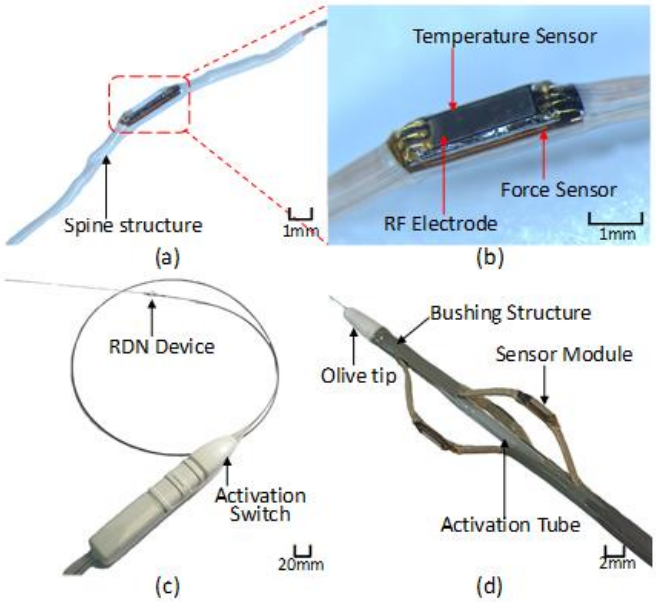

Fig. 4. Image of the assembled renal denervation (RDN) device. (a) Single spine structure; (b) enlarged image of the assembled spine structure; (c) RDN catheter; (d) RDN device in an "open" state.

A layer of piezoresistive ink is first added under the base of the MEMS-based sensor chip. The ink is cured at 150°C for 30 min. After the curing process, the MEMS-based sensor chip is stacked on the surface of the FPCB, and the wire-bonding process is performed to establish electrical connectivity. The wire-bond region is encapsulated with epoxy to prevent wire sweep.

In the next step, a 100-µm-thin layer of radiopaque film is attached onto the base of the FPCB. This film is visible under fluoroscopy and allows surgeons to determine the location of the RDN device inside the patient during the RDN procedure. Subsequently, the assembled structure is attached to a pre-bent memory alloy structure. After its attachment, 1.5-m-long enameled wires are soldered onto the FPCB bonding pads. These wires provide the electrical input and output signal of the temperature, force sensor, and RF electrode to the external circuit module and generator.

In the final step, the spine structure is formed using a polytetrafluoroethylene (PTFE) shrink tube to encapsulate the assembled device. The assembled structure is first inserted into the shrink tube. The shrink tube is then shrunk at 220°C to encapsulate the assembled structure. An opening is created in the PTFE tube to expose the MEMS-based sensor chip for temperature sensing and the RF ablation of the renal nerve.

After the single spine structure assembly is formed, the three assembled spine structures must be integrated with the catheter device. Each spine structure is inserted into its corresponding slot of bushing structures at both ends. An activation tube for deploying the three spine structures is inserted into the center of the bushing structure. This activation tube is connected to the RDN catheter activation switch to control the deployment of the RDN device. The deployment proceeds in five stages of opening, during which the maximum expansion of the three spine structures is 8 mm in diameter (Fig. 4b). The pre-bent memory alloy structure ensures the device maintain the desired mechanical shape upon deployment at different stages. An olive tip is inserted at the distal end of the catheter, and the insulated wires of the three spine structures are bundled and threaded through an 8-French catheter to connect to the external RF generator. Fig. 4d illustrates the assembled RDN catheter.

IV. Measurement Results and Discussion

A. MEMS-Based Temperature Sensor Testing

After the single spine structure assembly was completed, benchtop characterization of the MEMS-based sensor chip is conducted to validate the temperature sensor performance. The chip is first submerged in a saline solution bath with a temperature range from room temperature to 94°C. A calibrated thermocouple is used to validate the saline solution temperature. At each 14°C interval, the resistance output of the temperature-sensing element is recorded (Fig. 5).

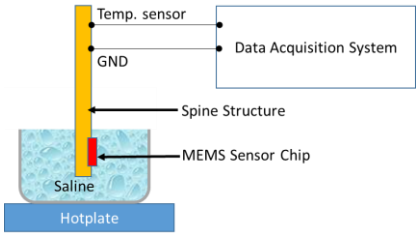

Fig. 5. Experimental setup for MEMS-based temperature sensor testing.

This testing procedure is conducted on five MEMS-based sensor chips; the average resistance values of the temperature-sensing elements are tabulated and plotted in Fig. 6, with a standard deviation of 2σ. The resistance of the MEMS-based temperature sensor is linearly proportional to the temperature, with a thermal coefficient of 2.832 x 10^{-3} / °C. This result validates the thin-film platinum-based temperature sensor. The fabricated 0.15um thick platinum-based temperature sensor is

comparable to a 0.2um thick platinum-based temperature sensor array with a thermal coefficient of 2.98 × 10^{-3} / °C [30].

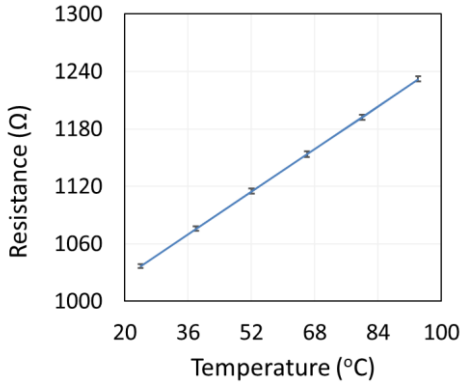

Fig. 6. MEMS-based temperature sensor testing result.

The temperature response of the MEMS-based sensor chip is then evaluated. The single spine structure is placed in a metal bowl filled with saline solution, which is placed on a metal grounding plate. Both the metal grounding plate and the MEMS-based ablation electrode are connected to the RF generator. Simultaneously, the MEMS-based temperature sensor is connected to a data acquisition unit to measure the temperature response (Fig. 7).

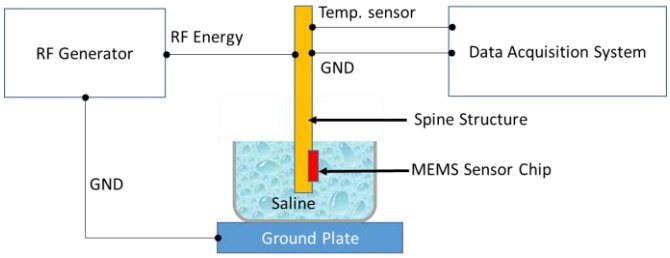

Fig. 7. Experimental setup for temperature response testing.

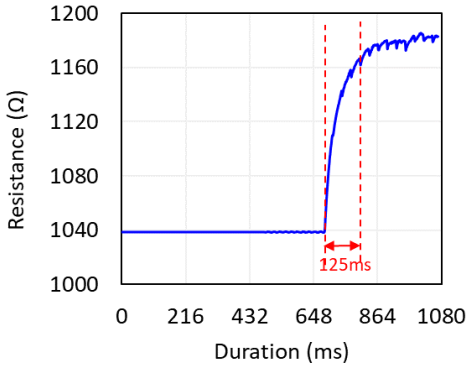

Fig. 8. Temperature response testing result.

To verify the temperature response of the MEMS sensor, 2 W of RF energy is supplied to the MEMS-based ablation electrode. The acquisition unit measures the resistance output of the thin-film platinum-based temperature sensor at a rate of 2 ms per data point. The MEMS-based sensor chip can achieve a response duration T_{90} of 125 ms, which is sufficient for the renal nerve ablation requirement of 500 ms (Fig. 8).

The durability of the RF ablation electrode is then verified. The study is conducted using the experimental setup illustrated in Fig. 7. In this study, 8 W of RF energy is supplied to the RF ablation electrode for 60 s. The supply of RF energy is then disabled for 60 s. This experiment is conducted for 32 cycles based on average ablation requirement for the renal denervation application [31]. The resistance of the temperature sensor is measured by the acquisition unit, and the results are processed and converted to temperature output. The results of the RF ablation electrode are presented in Fig. 9. The average temperature measurement at 8 W of RF power is 102.9°C, with a noise fluctuation of 12 Ω. There is no visible defect or electrode delamination issue observed after 32 cycles. The graph reveals that the temperature sensor drifts after each cycle. This may be caused by the multiple heating cycles, resulting in temperature increments in the saline solution during the experiment.

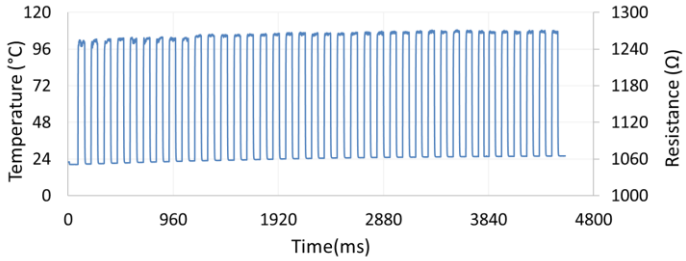

Fig. 9. RF ablation electrode durability test at an RF of 8 W for 32 cycles.

An ex vivo ablation study is then conducted to verify heater electrode ablation performance. A piece of meat is immersed in the saline solution and the spine structure with the MEMS-based sensor chip is placed in contact with the meat surface. The MEMS-based sensor chip is connected to the external RF generator (Fig. 10).

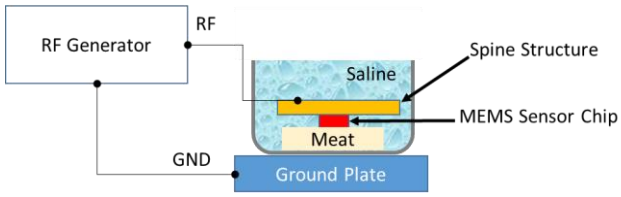

Fig. 10. Ex vivo ablation experimental setup.

RF power with a range of 0.5–9 W is supplied to the RF ablation electrode for 60 s. Fig. 11 presents the ablation marks on the piece of meat corresponding to the respective RF power supply. The optimal ablation marks on the piece of meat are from 1 to 1.5 W, and they have a width and length of 1.9 and 2 mm, respectively. Burn marks can be identified at an RF power of more than 2 W, indicating the overablation of flesh, which is undesirable for the RDN procedure.

In the subsequent benchtop characterization, the ablation temperature for an optimal RF power of 1 and 1.5 W was determined. The experimental setup is similar to that in Fig. 7. A graphical user interface that indicates the temperature sensor resistance and corresponding temperature is used instead of a data acquisition system. RF energies of 1 and 1.5 W are applied to the ablation electrode for 25 s. Fig. 12 presents the results. The average ablation temperature for an RF power of 1 and 1.5 W is 95°C and 103°C, respectively,

which is higher than the ablation temperature of 85°C required for successful nerve ablation. However, the ablation temperature for an RF power of 1 and 1.5 W is expected to be lower in an animal or a human individual because of the constant flow of blood in the artery.

(a)

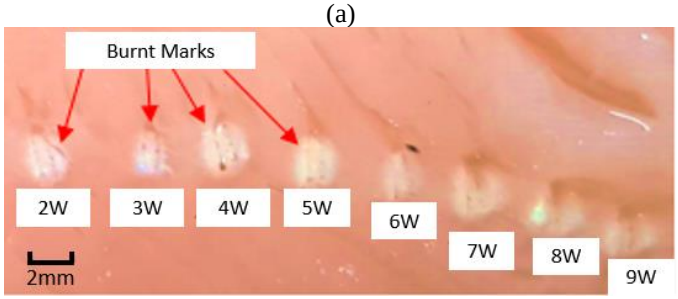

(b)

Fig. 11. Ex vivo RF electrode ablation studies using a piece of meat. (a) Ablation marks using an RF power of 0.5–0.9 W; (b) ablation marks with an RF of 1–9 W.

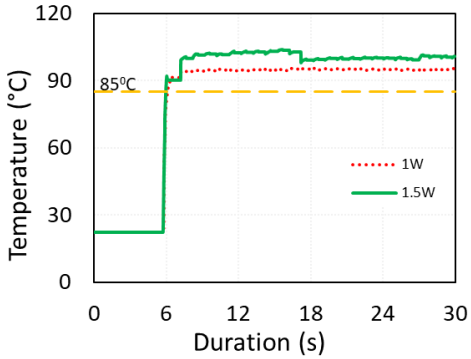

Fig. 12. Ablation tests at an RF of 1 and 1.5 W.

B. Force-Sensor Testing

The next benchtop test focuses on force-sensor characterization. In this experiment, the single spine structure is placed on a flat platform (Fig. 13). The platform moves in the direction of the *z*-axis until it is in contact with the force-gauge tip. The force-gauge tip is connected to a force gauge to measure the contact force between the gauge tip and MEMS-based sensor chip. The force-sensor testing range is 50–500 mN. The force-sensing readout corresponding to the contact force is measured using a multimeter. This testing procedure is conducted on five MEMS-based sensor chips; the average resistance values of the force-sensing elements are tabulated and plotted in Fig. 14, with a standard deviation of 2σ.

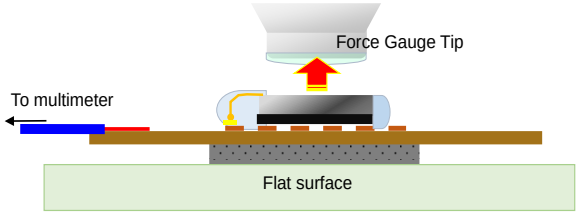

Fig. 13. Force-sensor experimental setup.

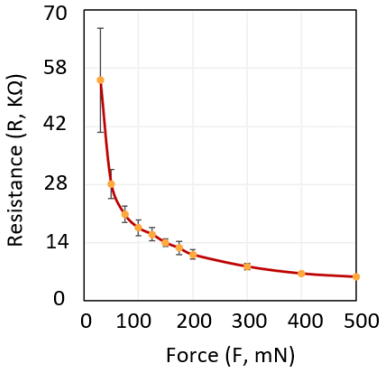

Fig. 14. Force-sensor benchtop results.

The force sensor does not register a resistance reading when force is not applied to the sensing element. When force is applied, the resistance of the sensing element decreases with the amount of force applied. The minimum activation force of the force sensor is 50 mN with a resolution of 50 mN. The force sensor is tested up to 500 mN of applied contact force.

The next test focuses on the hysteresis effect of the force sensor on the assembled catheter. The hysteresis effect is predominantly observed in a physical sensor. To validate this effect, a force loading and unloading procedure is conducted on the assembled catheter using the setup in Fig. 15. The hysteresis study is conducted on the three force sensors of an assembled catheter. One of the force sensor modules is secured on the jig with a force gauge. The force gauge is used to load the sensor up to 500 mN by gradually increasing it from 50 to 150 and 350 mN. The resistance values at each test data point are recorded. The load on the sensor is then gradually decreased from 500 to 350, 150, and 50 mN. The resistance values at each test data point are recorded. Each force sensor undergoes three cycles of loading and unloading. The average resistance values are tabulated and plotted in Fig. 16.

(a)

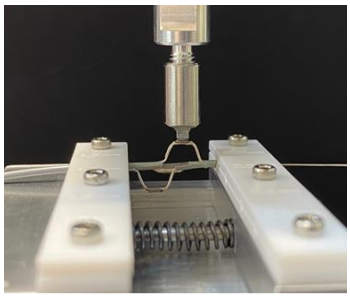

(b)

Fig. 15. Hysteresis test setup. (a) Force-gauge setup; (b) tip of the force gauge on the force-sensor module

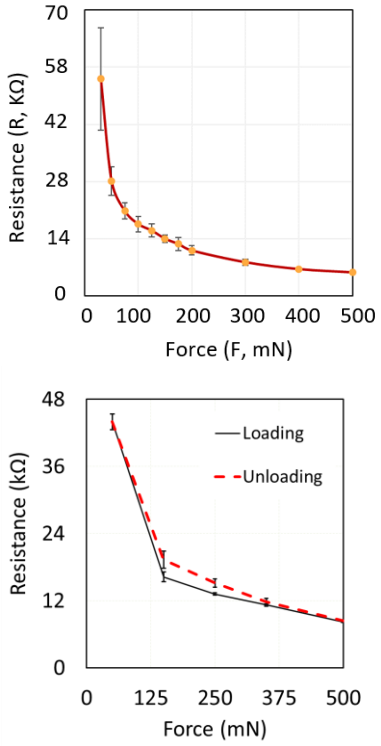

Fig. 16. Hysteresis test result.

Fig. 16 illustrates the loaded force in mN versus the resistance in kΩ of the assembled force-sensor module. The force-sensor modules are verified to be functional between the force ranges of 50 and 500 mN. The difference in resistance caused by the force applied or released during loading and unloading (hysteresis), respectively, is greater at 150 and 250 mN. This could be because of the continuous force loading at 150 and 250 mN, which is different from the endpoint resistance values obtained at 50 and 500 mN. Nevertheless, the average error in the resistance reading resulting from hysteresis is approximately 0.7 kΩ, which is negligible and overshadowed by the sensor performance.

Because the catheter must be inserted into a patient's arteries, the catheter's force-sensor performance in fluid conditions must be validated. A baseline testing scenario of catheter activation in air is conducted. The catheter is first gradually activated from its closed state, OP 0, to its fully opened state, OP 5. The resistance value of the force sensor is recorded for each opening state (Table 1).

TABLE 1
RESULTS OF CATHETER ACTIVATION TEST

Opening / Scenarios	Force Sensor Resistance (kΩ)					
	OP 0	OP 1	OP 2	OP 3	OP 4	OP 5
1: In Air	Open	Open	Open	Open	Open	Open
2: In Tube (W/O Saline)	Open	Open	Open	Open	135.7	64.8
3: In Tube (With Saline)	Open	Open	Open	252.3	133.1	63.2

Fig. 17 depicts the test setup in air for the closed and fully opened states. Because no force is applied to the force-sensing element, resistance values cannot be observed in all the opening states. This result demonstrates that the force-sensor readout is independent of the activation of the catheter in the assembly package.

After the force-sensor performance is verified in air, the catheter is inserted into a tube with an inner diameter of 3 mm. The catheter is gradually activated from OP 0 to OP 5 (Fig. 18). The resistance value at each opening state is recorded (Table 1). In this study, the resistance change in the force-sensing element of 135.7 and 64.87 kΩ is observed for OP4 and OP 5, respectively, indicating that the force sensor is in contact with the inner wall of the tube. Thus, the resistance value of the force-sensing element changes considerably.

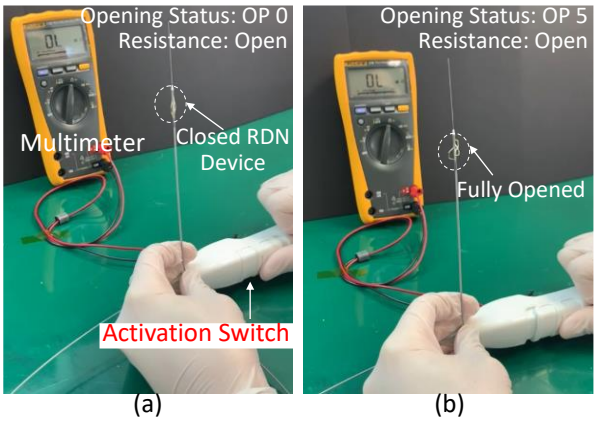

Fig. 17. Catheter testing in air. (a) RDN device in a closed state, OP 0; (b) RDN device in a fully opened state, OP 5.

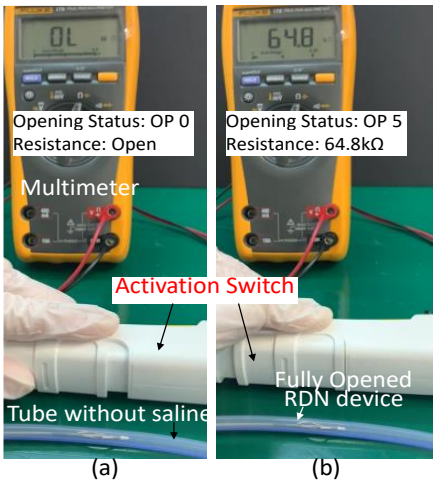

Fig. 18. Catheter testing in a hallow tube. (a) RDN device in a closed state, OP 0; (b) RDN device in a fully opened state, OP 5.

In the next testing scenario, the performance of the force-sensor module in saline solution is validated. With the same setup depicted in Fig. 18, saline solution is introduced into the tube for a fluid environment simulation test as shown in Fig. 19. The resistance value of the force sensors for different scenarios and opening states are tabulated in Table 1.

In this study, a high resistance value of approximately 3.4 MΩ is observed at OP 0 to partial open state OP2. These results, which differ from those for the air and tube tests

without saline solution, may be caused by the saline solution applying pressure to the force sensor. The resistance value at OP 5 is measured at 63.2 kΩ, which is approximately 50 times that at OP 0. Therefore, the resistance values at OP 0 to OP 2 are considered to be negligible, with no contact force between the tube and force sensor. The resistance values of OP 4 and OP 5 measured in the saline solution are consistent with the reading measured in the tube without saline solution as shown in Fig. 20.

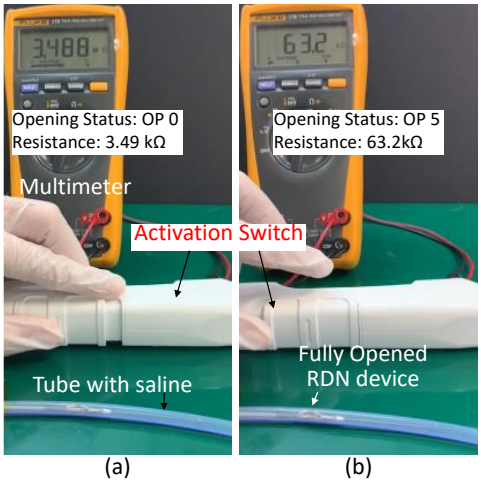

Fig. 19. Catheter testing in a tube with saline solution. (a) RDN device in a closed state, OP 0; (b) RDN device in a fully opened state, OP 5.

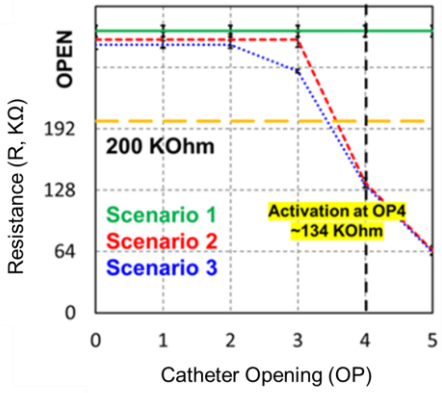

Fig. 20. Catheter levels force-sensor verification result for different scenarios.

The functionality of the temperature sensor with the force sensor is then verified. For this study, the MEMS-based sensor chip is connected to the GUI-equipped application. The MEMS-based sensor chip is placed in contact with a finger for 30 s. The temperature-sensing feature of the MEMS-based sensor chip measures the finger temperature, and the force sensor measures the contact force applied by the finger. The resistance readout for both temperature and force sensor is measured using the GUI; the temperature is displayed in degrees Celsius and the force is displayed in millinewtons (Fig. 21). The MEMS-based temperature indicates that the finger temperature is 32°C and the force applied is approximately 113 mN.

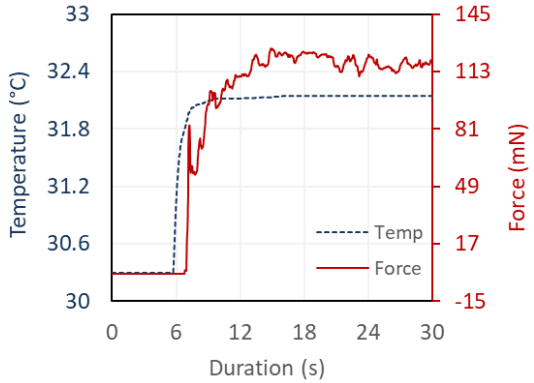

Fig. 21. Temperature and force-sensor test results with the finger touching the MEMS-based sensor chip.

V. Conclusion

This paper presented the development of a multifunctional catheter to treat resistant hypertension through the ablation of an overactive renal nerve. The multifunctional catheter comprises a MEMS-based temperature sensor, a thin-film ablation electrode, and a printable force-sensor module. The performance of the multifunctional catheter was validated through benchtop characterization tests and ex vivo animal models.

In addition, benchtop characterization tests were conducted to verify the temperature, force-sensor, and ablation electrode performance. The MEMS-based temperature sensor was validated at 25°C–94°C, with a temperature response time of 125 ms. A durability test was conducted on the ablation electrode at an RF power of 8 W for 32 cycles. No visible damage to the ablation electrode was observed. An ex vivo ablation test using meat was performed, and the optimal RF power for ablation was reported to be in the range of 1–1.5 W.

Characterization tests were conducted on both the single spine system and assembled catheter. A printable force-sensing element exhibited a decreasing exponential trend with increasing applied force from 50 to 500 mN. The minimum force resolution was 50 mN with a hysteresis error of 0.7 kΩ. The force-sensor module in the assembled catheter underwent a catheter activation procedure in air and a tube with and without saline solution. These studies verified that the assembled force-sensor module was independent of catheter activation. The force-sensing resistance readout for an opening status of OP4 and OP 5 in a tube was consistent with and without saline solution. This validated the force-sensor performance under fluid conditions.

System-level integration with the assembled catheter, GUI, and external RF generator indicated an ablation temperature measurement of 95°C and 103°C at 1 and 1.5 W of supplied RF power, respectively. Concurrent validation of the temperature sensor and force sensor was performed using a finger-touching procedure, where the finger comes in contact with surface of the MEMS-based sensor chip. The RDN device can measure a finger temperature of 32°C with 113 mN of applied force. In future studies, the performance of the multifunctional RDN device should be validated in an animal model.

VI. REFERENCES

[1] Lucas Lauder, Michael Böhm and Felix Mahfoud, "The current status of renal denervation for the treatment of arterial hypertension," Progress in Cardiovascular Diseases 65, pp.76–83, 2021.

[2] Charles Faselis, Michael Doumas, and Vasilios Papademetriou, "Common Secondary Causes of Resistant Hypertension and Rational for Treatment," International Journal of Hypertension, vol 2011, pp.1-7, 2011.

[3] Eduardo Pimenta and David A. Calhoun, "Resistant Hypertension: Incidence, Prevalence, and Prognosis," Circulation, vol. 125, no. 13, 2012.

[4] Williams B., Mancia G., Spiering W., Agabiti Rosei E., Azizi M., Burnier M., Clement D., Coca A., de Simone G., Dominiczak A., Kahan T., Mahfoud F, Redon J, Ruilope L, Zanchetti A, Kerins M, E Kjeldsen S, Kreutz R., Laurent S., Lip G. Y. H., McManus R., Narkiewicz K., Ruschitzka F., Schmieder R., Shlyakhto E., Tsioufis C., Aboyans V., Desormais I. and ESC Scientific Document Group, "2018 ESC/ESH Guidelines for the management of arterial hypertension," European Heart Journal, vol. 39, no.33, pp.3021–104, 2018.

[5] Calhoun D. A., Jones D., Textor S, Goff D. C., Murphy T. P., Toto R. D., White A., Cushman W. C., White W., Sica D., Ferdinand K., Giles T. D., Falkner B. and Carey R. M., "Resistant hypertension: diagnosis, evaluation, and treatment: a scientific statement from the American Heart Association Professional Education Committee of the Council for High Blood Pressure Research," Hypertension, vol. 117, no. 25, pp. e510–e526, 2008.

[6] J. P. Garg, W. J. Elliott, A. Folker, M. Izhar, and H. R. Black, "Resistant hypertension revisited: a comparison of two university-based cohorts," American Journal of Hypertension, vol. 18, no. 5, pp. 619–626, 2005.

[7] D. P. Papadopoulos and V. Papademetriou, "Resistant hypertension: diagnosis and management," Journal of Cardiovascular Pharmacology and Therapeutics, vol. 11, no. 2, pp. 113–118, 2006.

[8] P. A. Sarafidis and G. L. Bakris, "Resistant hypertension. An overview of evaluation and treatment," Journal of the American College of Cardiology, vol. 52, no. 22, pp. 1749– 1757, 2008.

[9] M. H. Alderman, "Resistant hypertension: a clinical syndrome in search of a definition," American Journal of Hypertension, vol. 21, no. 9, pp. 965–966, 2008.

[10] M. Moser, W. Cushman, and J. Handler, "Resistant or difficult-to-treat hypertension," Journal of Clinical Hypertension, vol. 8, no. 6, pp. 434–440, 2006.

[11] J. Amar, "Patients with resistant hypertension," Journal of Hypertension, vol. 25, pp. S3–S6, 2007.

[12] M. Epstein, "Resistant hypertension: prevalence and evolving concepts," Journal of Clinical Hypertension, vol. 9, no. 1, pp.2–6, 2007.

[13] R. Pisoni, M. I. Ahmed, and D. A. Calhoun, "Characterization and treatment of resistant hypertension," Current Cardiology Reports, vol. 11, no. 6, pp. 407–413, 2009.

[14] Eline H. Groenland and Wilko Spiering, "Baroreflex Amplification and Carotid Body Modulation for the Treatment of Resistant Hypertension," Current Hypertension Reports, 22: 27, 2020.

[15] Raffaella Greco and Eugenio Greco, "Carotid baroreceptor stimulation to treat resistant hypertension," ESC Council on Cardiology Practice, vol.11, 2013.

[16] Uppuluri S.C., Storozynsky E., Bisognano J.D., "Baroreflex device therapy in the treatment of hypertension," Current Hypertension Reports,11, pp.69–75, 2009.

[17] Carlsten A., Folkow B., Grimby G., Hamberger Ca. and Thulesius O., "Cardiovascular effects of direct stimulation of the carotid sinus nerve in man," Acta Physiol Scand, 44, pp.138–145, 1958.

[18] Lohmeier T.E., Hildebrandt D.A. and Warren S., "Recent insights into the interactions between the baroreflex and the kidneys in hypertension," Am J Physiol Regul Integr Comp Physiol., 288, pp.828–836, 2005.

[19] Salman I.M., Ameer O.Z., McMurray S., Hassan S.F., Sridhar A., Lewis S.J. and Hsieh Y.H., "Low intensity stimulation of aortic baroreceptor afferent fibers as a potential therapeutic alternative for hypertension treatment," Sci Rep., 12(1):12242, 2022.

[20] Eline H. Groenland and Wilko Spiering, "Baroreflex Amplification and Carotid Body Modulation for the Treatment of Resistant Hypertension," Current Hypertension Reports, 22: 27, 2020.

[21] Lohmeier TE, Hall JE, "Device-Based Neuromodulation for Resistant Hypertension Therapy," Circ Res., 124(7), pp. 1071–1093, 2019.

[22] Hoppe U.C., Brandt M.C., Wachter R., Beige J., Rump L.C., Kroon A.A., Cates A.W., Lovett E.G. and Haller H., "Minimally invasive system for baroreflex activation therapy chronically lowers blood pressure with pacemaker-like safety profile: results from the Barostim neo trial," J Am Soc Hypertens, 6(4), pp. 270–276, 2012.

[23] Spiering W, Williams B, Van der Heyden J, Kleef Van M, Rob Lo, Versmissen J "Endovascular baroreflex amplification for resistant hypertension: a safety and proof-of-principle clinical study," Lancet, 390(10113), pp.2655–2661, 2017.

[24] Markus P Schlaich, "Renal Sympathetic Denervation: A Viable Option for Treating Resistant Hypertension," Am J Hypertens, 30(9), pp.847-856, 2017.

[25] R. Lim, M.Y. Cheng, W. Chen, D. Choong, J.H. Park, J. Oh, S. Seung and EJ. Park, "Development of Integrated Thermistor Sensor and Heating Electrode for Renal Denervation Procedure," 2018 IEEE 68th Electronic Components and Technology Conference (ECTC), pp. 777-782, 2018.

[26] Research and Markets, "Renal Denervation Market Size, Share & Trends Analysis Report By Technology (Micro-Infusion, Ultrasound, Radiofrequency Based), By Region (Europe, APAC, MEA, NorthAmerica), And Segment Forecasts, 2018 – 2026," https://www.researchandmarkets.com/reports/4668018/renal-denervation-market-size-share-and-trends (Assessed June 19, 2023).

[27] Mahfoud F, Böhm M, Schmieder R, Narkiewicz K, Ewen S, Ruilope L, Schlaich M, Williams B, Fahy M, Mancia G, "Effects of renal denervation on kidney function and long-term outcomes: 3-year follow-up from the global SYMPLICITY registry," Eur Heart J, 40(42), pp.3474-3482, 2019.

[28] S. B. N. Gourikutty, D. Choong, R. Lim, M.R.N.B. Damalerio, J. Oh, Y. Kim, I. Bae, M.Y. Cheng, "Temperature detection system for Renal Denervation Catheter application," 2020 IEEE 22nd Electronics Packaging Technology Conference (EPTC), pp. 198-202, 2020.

[29] Thomas Geninatti, Giacomo Bruno, Bernardo Barile, R Lyle Hood, Marco Farina, Jeffrey Schmulen, Giancarlo Canavese, Alessandro Grattoni, "Impedance characterization, degradation, and in vitro biocompatibility for platinum electrodes on BioMEMS," Biomedical Microdevices, pp.17-24, 2015.

[30] Mark Schepperle, Muhannad Ghanam , Andreas Bucherer, Timo Gerach, Peter Woias, "Noninvasive platinum thin-film microheater/temperature sensor array for predicting and controlling flow boiling in microchannels," Sensors and Actuators A: Physical, vol. 345, 113811, 2022.

[31] Sara I. Al Raisi, Michael T. Barry, Pierre Qian, Abhishek Bhaskaran, Jim Pouliopoulos, Pramesh Kovoor, "Comparison of new-generation renal artery denervation systems: assessing lesion size and thermodynamics using a thermochromic liquid crystal phantom model," EuroIntervention, 13, pp. 1242-1247, 2017.

Ruiqi Lim received the B.Eng. degree in electrical and electronics engineering from Nanyang Technological University (NTU), Singapore, in 2008. Since 2008, she has been with the Institute of Microelectronics, A*STAR, Singapore. Her research interest is mainly in substrate layout design, biocompatible packaging, and characterization for biomedical applications.

Maria Ramona Ninfa B. Damalerio received the B.Sc. degree in Electronics and Communications Engineering from University of St. La Salle, Bacolod City, Philippines, in 1997. She worked for semiconductor industry for 13 years before joining Institute of Mircoelectronics, A*STAR, Singapore in 2013. Her research interest is mainly in flexible electronics, packaging, and characterization for biomedical applications.

Musafargani Sikkandhar received the M.Sc. degree in Biomedical Engineering in 2018 from Nanyang Technological University, Singapore. He is currently working as Senior Research Engineer at Institute of Microelectronics, A*STAR, Singapore. His expertise includes semiconductor process development, healthcare sensor development and neurophysiological study.

James YAP Ven Wee received the B.Eng. degree in Mechanical Engineering from Universiti Tun Hussein Onn, Malaysia, in 2010. He worked for product research and development industry for 8 years before joining Institute of Microelectronics, A*STAR, Singapore in 2020. His research interest is mainly in device integration, packaging, and characterization for biomedical applications.

Ming-Yuan CHENG Dr Ming-Yuan Cheng is currently the head of Medtech department at the Institute of Microelectronics (IME). He received the Ph.D. degree from National Taiwan University, Taiwan, all in mechanical engineering. Dr Cheng holds 6 grant patents and published more than 100 research papers. He has more than 12 years of experience in microelectromechanical system, implantable medical device, bio-packaging, flexible electronics, and miniaturized electronics in MedTech's application. His main interests are in product prototype development and commercialization of research outcomes.